Inelastic vibrational bulk and surface losses of swift electrons in ionic nanostructures

Ulrich Hohenester,[1,*] Andreas Trügler,[1] Philip E. Batson,[2] and Maureen J. Lagos[2,3]
[1]*Institute of Physics, University of Graz, Universitätsplatz 5, 8010 Graz, Austria*
[2]*Department of Materials Science and Engineering, Department of Physics and Astronomy, Rutgers University, Piscataway, New Jersey 08854, USA*
[3]*Department of Materials Science and Engineering, McMaster University, Hamilton, Ontario L8S 4L7, Canada*

(Received 11 December 2017; revised manuscript received 27 March 2018; published 13 April 2018)

In a recent paper [Lagos *et al.*, Nature (London) **543**, 533 (2017)] we have used electron energy loss spectroscopy with sub-10 meV energy and atomic spatial resolution to map optical and acoustic, bulk and surface vibrational modes in magnesium oxide nanocubes. We found that a local dielectric description works well for the simulation of aloof geometries, similar to related work for surface plasmons and surface plasmon polaritons, while for intersecting geometries such a description fails to reproduce the rich spectral features associated with excitation of bulk acoustic and optical phonons. To account for scatterings with a finite momentum exchange, in this paper we investigate molecular and lattice dynamics simulations of bulk losses in magnesium-oxide nanocubes using a rigid-ion description and investigate the loss spectra for intersecting electron beams. From our analysis we can evaluate the capability of electron energy loss spectroscopy for the investigation of phonon modes at the nanoscale, and we discuss shortcomings of our simplified approach as well as directions for future investigations.

DOI: 10.1103/PhysRevB.97.165418

I. INTRODUCTION

The recent development of a new generation of monochromators in electron microscopes has triggered spatially-resolved studies of vibrational excitations in materials using atom-sized electron probes [1]. As a result, there have been theoretical and experimental reports on vibrational losses by swift electrons in a small volume of matter. For instance, the mapping of vibrational excitations in MgO nanocubes was obtained [2]. It was demonstrated that a swift electron can couple to both bulk and surface vibrational modes, with scattering signals located within the cube and near the cube surfaces, respectively. From the theory point of view, several quantum models describing the physical aspects of the inelastic electron scattering by phonons in infinite solids [3–6] and by vibrational modes in molecular systems [7,8] have been reported. In spite of this significant progress, the full understanding of the vibrational inelastic electron scattering from nanosized systems remains to be achieved. At the nanoscale, shape and size lead to the generation of new surface vibrational (polariton) modes [9,10] which play an important role for tuning the vibrational response of nanostructures.

It is well known that the f-sum rule points out the interplay between surface and bulk scattering in the dynamic form factor [11]. This relationship between surface and bulk scattering can be illustrated in the Begrenzung effect, and it is useful for the understanding of scattering modulations near nanoscale boundaries. It also might lead to the discovery of new short-wavelength surface modes, since variations in the bulk scattering associated with the excitation of short-wavelength bulk phonon modes near surfaces were reported [2]. As a matter of fact, two different types of highly-localized microscopic surface modes were predicted in ionic surfaces [12–14], suggesting that bulk scattering variations might occur within atom-scale distances near surfaces in order to fulfill the sum rule. Therefore, a scattering theory accounting for finite size effects on the excitations of both long and short-wavelength phonon modes is still needed. Also, the sum rules driving the interplay between surface and bulk scattering (Begrenzung effect) might lead to the prediction of new surface short-wavelength modes, resulting in atom-scale variations of bulk and surface scattering signals near surfaces. Thus, a model accounting for size and shape effects on the excitations of both long and short-wavelength phonon modes is needed.

The dielectric theory, in principle, should account for the description of the physics of the inelastic vibrational loss scattering of finite-size objects. This method usually requires the knowledge of the frequency and wave-vector dependent dielectric material function. However, this represents an important limitation in the straightforward application of the theory due to lack of such information, because most of the available bulk dielectric data are limited to the long wavelength range (wave number $q \to 0$). Thus, most of the spectroscopy studies of nanostructures were so far limited to long-wavelength vibrational excitations [15].

The purpose of this work is to present an alternative semiclassical model of the vibrational inelastic scattering by relativistic electrons in bulk materials and finite nanostructures, which considers all phonon modes within the entire Brillouin zone. Our theory deals with the atomistic aspects of phonon excitations within the lattice dynamics and molecular dynamics approaches. The calculation of inelastic scattering cross sections relies on the quantum aspects of the scattering, but our model presents a further derivation to establish a relationship with elements of classical models. A single formula is derived

*ulrich.hohenester@uni-graz.at

which describes the coupling between the fast electron and the phonon modes, including nondipole interactions. One advantage of our approach over the local dielectric formalism is the description of the inelastic scattering from both acoustic and optical modes, and the evaluation of their relative contribution to the scattering across the Brillouin zone. Also, our model enables us to evaluate scattering probabilities of the probe with varying location within the nanostructure. In particular, this allows us to study short-wavelength excitations within the solid and near surfaces in atom-sized systems, where the local dielectric approach is known to break down [16].

We have used our theory to calculate the inelastic scattering losses in a MgO cube in order to compare it with available experimental data. In order to compute the scattering probability, we have used the rigid-ion approximation [17,18] for the description of the lattice dynamics of the cube. In principle, one can use more precise values derived from first-principles calculations as input parameters. In this paper, we discuss the range of validity of our approximations, highlight the important parameters to be considered, and point out possible directions for future work.

We have organized this paper as follows. In Sec. II we develop our theory for the computation of bulk and surface phonon losses using either a local dielectric description or molecular and lattice dynamics simulations based on a rigid ion model description. The validity of the rigid-ion approximation underlying our approach is briefly discussed in Sec. III. In Sec. IV we present results for the different model descriptions and identify the pertinent physical mechanisms underlying bulk losses in ionic crystals. Finally, in Sec. V we summarize and provide a critical discussion of our approach. Some details of our theoretical framework have been moved to the various appendices.

II. THEORY

In this section we present our theory for the description of electron energy loss spectroscopy (EELS) for ionic nanostructures. We closely follow the original work of Ritchie [19], see also Refs. [20,21] for more details, and introduce only a few modifications to explicitly account for phonon rather than plasmon excitations. A full quantum-mechanical approach for EELS of phonon excitations has been recently developed and applied to bulk crystals [6]. However, for clarity we here give precedence to the more simple and transparent semiclassical approach.

The interaction between the swift electron at position $\boldsymbol{r}$ and the ionic crystal with charge density $\rho_I(\boldsymbol{r}')$ is described by the Hamiltonian

$$H' = -\int \frac{e\rho_I(\boldsymbol{r}')}{|\boldsymbol{r}-\boldsymbol{r}'|}\,d^3r'\,. \tag{1}$$

Here $-e$ is the electron charge and we use Gauss units throughout. Within the rigid-ion model, which we will use later in this paper, the ions are described as pointlike particles, located at impact parameter values $\boldsymbol{R}_j$ and with the effective charge eZ_j, and the charge distribution becomes

$$\rho_I(\boldsymbol{r}') = \sum_j eZ_j\,\delta(\boldsymbol{r}'-\boldsymbol{R}_j)\,. \tag{2}$$

According to Fermi's golden rule we can write the transition rate between the initial and final states $\psi_i(\boldsymbol{r})$ and $\psi_f(\boldsymbol{r})$ of the swift electron, with energies ε_i and ε_f, respectively, in the usual form

$$\gamma = \frac{2\pi e^2}{\hbar}\sum_{f,n}\left|\int \frac{\psi_f^*(\boldsymbol{r})\psi_i(\boldsymbol{r})\langle n|\rho_I(\boldsymbol{r}')|0\rangle}{|\boldsymbol{r}-\boldsymbol{r}'|}\right|^2 \times\delta(\varepsilon_f-\varepsilon_i+\hbar\omega_n-\hbar\omega_0)\,. \tag{3}$$

$\hbar$ is Planck's reduced constant, $|0\rangle$ and $|n\rangle$ denote the ground- and excited states of the ionic system, respectively, and $\hbar\omega_0$ and $\hbar\omega_n$ are the corresponding energies. In the above equation we have assumed that initially the ionic system resides in the ground state, although our approach would easily allow for an initial thermal distribution and consider for the swift electron only single scattering events.

To render Eq. (3) suitable for an electrodynamics description, we introduce the susceptibility [21]

$$\Im\mathrm{m}[\chi(\boldsymbol{r},\boldsymbol{r}',\omega)] = -\frac{\pi}{\hbar}\sum_n \langle 0|\rho_I(\boldsymbol{r})|n\rangle\langle n|\rho_I(\boldsymbol{r}')|0\rangle\,\delta(\hbar\omega+\hbar\omega_n-\hbar\omega_0), \tag{4}$$

which is also known as the density-density correlation function or the dynamic form factor [22] (the latter is usually defined without the factor $\hbar$ in the denominator). We next decompose the transition rate into loss energies according to $\gamma=\int_0^\infty \gamma(\hbar\omega)\,d\hbar\omega$ and follow the procedure outlined in Refs. [20,21] and briefly sketched in Appendix A, in order to arrive at the central equation for computing the electron energy loss probability

$$P(\hbar\omega) = \frac{1}{\pi\hbar\omega}\int \Re\mathrm{e}[\boldsymbol{E}_{\mathrm{el}}^*(\boldsymbol{r},\omega)\cdot\boldsymbol{J}_{\mathrm{ind}}(\boldsymbol{r},\omega)]\,d^3r\,. \tag{5}$$

In brief, Eq. (5) describes the electron loss probability of a swift electron to an ionic nanosystem through coupling between the swift electron's electric field $\boldsymbol{E}_{\mathrm{el}}$ and the induced polarization current $\boldsymbol{J}_{\mathrm{ind}}$ of the ionic crystal. This expression can be used for both local dielectric descriptions as well as atomistic descriptions at various levels of sophistication. In the latter case, $\boldsymbol{J}_{\mathrm{ind}}$ has to be related to the lattice displacements of the ions.

A. Lattice dynamics

In the semiclassical lattice dynamics approach we introduce an explicit description of the phonon dynamics in terms of the so-called rigid-ion model [17,18]. We consider an infinite ionic crystal with ions located at positions

$$\boldsymbol{R}(\kappa,\ell) = \boldsymbol{R}_\ell + \boldsymbol{r}_\kappa + \boldsymbol{u}(\kappa,\ell)\,.$$

Here $\boldsymbol{R}_\ell$ points to the ℓth unit cell and $\boldsymbol{r}_\kappa$ to the κth ion within a unit cell, and $\boldsymbol{u}(\kappa,\ell)$ is the displacement from the equilibrium positions. Expressing for a harmonic time dependence $e^{-i\omega t}\boldsymbol{u}$ the current distribution in the form $\boldsymbol{J}_{\mathrm{ind}}(\kappa,\ell) = -i\omega\sum_{\kappa\ell}\boldsymbol{u}(\kappa,\ell)\,eZ_\kappa\delta(\boldsymbol{r}-\boldsymbol{R}_\ell-\boldsymbol{r}_\kappa)$, the electron energy loss probability of Eq. (5) becomes

$$P(\hbar\omega) = \frac{1}{\pi\hbar}\,\Im\mathrm{m}\left[\sum_{\kappa\ell}\boldsymbol{E}_{\mathrm{el}}^*(\boldsymbol{R}_\ell+\boldsymbol{r}_\kappa,\omega)\cdot eZ_\kappa\boldsymbol{u}(\kappa,\ell)\right]. \tag{6}$$

As discussed in more detail in Appendix C, we can expand the ion displacements in terms of the phonon eigenmodes $\boldsymbol{\xi}_\lambda(\kappa,\boldsymbol{q})$ with energy $\hbar\omega_{\boldsymbol{q}\lambda}$ through

$$\boldsymbol{u}(\kappa,\ell) = M_\kappa^{-1/2} \sum_{\boldsymbol{q}\lambda} e^{i\boldsymbol{q}\cdot\boldsymbol{R}_\ell} \frac{F_\lambda(\boldsymbol{q})}{\omega_{\boldsymbol{q}\lambda}^2 - \omega(\omega+i\eta)} \boldsymbol{\xi}_\lambda(\kappa,\boldsymbol{q}), \quad (7)$$

where $\boldsymbol{q}$ is the phonon wave vector and the term $F_\lambda(\boldsymbol{q}) = \sum_\kappa M_\kappa^{-1/2} e Z_\kappa \boldsymbol{\xi}_\lambda^*(\kappa,\boldsymbol{q}) \cdot \boldsymbol{E}(\kappa,\boldsymbol{q})$ describes how efficiently the swift electron couples to the phonons. M_κ is the ion mass, η is a small damping constant accounting for environment couplings, and the z component of the wave vector is given by $q_z = \frac{\omega}{v}$ because of kinematic constraints. Inserting Eq. (7) into Eq. (6) gives

$$P(\hbar\omega) = \frac{N}{\pi\hbar} \sum_{\boldsymbol{q}\lambda} \Im\mathrm{m}\left[\frac{|F_\lambda(\boldsymbol{q})|^2}{\omega_{\boldsymbol{q}\lambda}^2 - \omega(\omega+i\eta)}\right], \quad (8)$$

where N is the total number of unit cells. We finally investigate the continuum limit of Eq. (8). We first factorize $F_\lambda(\boldsymbol{q}) = \frac{ie}{\pi v}\left(\frac{2\pi}{L}\right)^2 \mathcal{F}_\lambda(\boldsymbol{q})$ into a constant prefactor together with

$$\mathcal{F}_\lambda(\boldsymbol{q}) = \sum_{\kappa,\boldsymbol{G}_\perp} M_\kappa^{-1/2} e Z_\kappa \boldsymbol{\xi}_\lambda^*(\kappa,\boldsymbol{q}) \cdot e^{i(\boldsymbol{q}+\boldsymbol{G})\cdot(\boldsymbol{r}_\kappa - \boldsymbol{R}_0)} \times \left[\frac{\boldsymbol{q}+\boldsymbol{G}-k\frac{\boldsymbol{v}}{c}}{|\boldsymbol{q}+\boldsymbol{G}|^2 - k^2}\right], \quad (9)$$

which describes the coupling between the electric field of the swift electron and the λth phonon eigenmode with wave number $\boldsymbol{q}$ (for the reciprocal lattice vector in the electron propagation direction z we set $G_z = 0$, as discussed in Appendix C). Using these definitions and performing the continuum limit in Eq. (8) we are then led to

$$P(\hbar\omega) = \frac{1}{\pi\hbar}\frac{e^2}{\pi^2 v^2}\left(\frac{2\pi}{L}\right)^2\left(\frac{L^3}{\Omega_0}\right) \times \sum_\lambda \int_{BZ} \Im\mathrm{m}\left[\frac{|\mathcal{F}_\lambda(\boldsymbol{q})|^2}{\omega_{\boldsymbol{q}\lambda}^2 - \omega(\omega+i\eta)}\right] d^2q_\perp,$$

where we have used $L^3 = N\Omega_0$, with Ω_0 being the volume of a crystal unit cell, and the integration of the wave vector $\boldsymbol{q}_\perp$ perpendicular to the electron propagation direction extends over the values within the first Brillouin zone. Thus, we are led to

$$P(\hbar\omega) = \frac{4e^2 L}{\pi\hbar v^2 \Omega_0} \sum_\lambda \int_{BZ} \Im\mathrm{m}\left[\frac{|\mathcal{F}_\lambda(\boldsymbol{q})|^2}{\omega_{\boldsymbol{q}\lambda}^2 - \omega(\omega+i\eta)}\right] d^2q_\perp. \quad (10)$$

This is the central expression of this section relating the energy loss probability to the phonon energies $\hbar\omega_{\boldsymbol{q}\lambda}$ and eigenmodes $\boldsymbol{\xi}_\lambda(\kappa,\boldsymbol{q})$.

Let us analyze the different contributions to Eq. (10) in slightly more detail, in particular in the $q \to 0$ limit which is relevant for long-range Coulomb interactions. Here the matrix elements $\mathcal{F}_\lambda(\boldsymbol{q})$ depend on the inner product $\boldsymbol{\xi}_\lambda^*(\kappa,\boldsymbol{q}) \cdot \boldsymbol{q}$ between the phonon eigenmodes and the wave vector $\boldsymbol{q}$, which is strongest for longitudinal phonons and weak for transversal phonon modes, whereas the magnitude of the matrix elements scales as $\sim 1/q$. In overall, the loss probability approximately scales as $\int |\mathcal{F}|^2\, dq_\perp \sim \int q\, dq/q^2 \sim \ln q$, with the lower integration limit ω/v given by the kinematic constraints and the upper limit q_c by the acceptance angle of the electron collector, see Eq. (14) below for a corresponding expression within the local dielectric framework. At finite temperature the loss probability should contain an additional factor $1 + n(\hbar\omega_{\boldsymbol{q}\lambda})$, with n being the Bose-Einstein distribution function, to account for thermal occupation of phonons. The interpretation of Eq. (10) becomes more difficult for electron trajectories located closer to the atom columns, where a larger portion of the Brillouin zone contributes to the loss probability, as will be discussed in more detail in Sec. IV.

B. Molecular dynamics

To describe the scattering in finite nanostructures, we additionally performed molecular dynamics (MD) simulations which are conceptually more simple but computationally more demanding, and thus restricted to sufficiently small nanosystems. The basic idea is to approximate the ions in the crystal by a number of pointlike particles with mass M_j and charge eZ_j, which are located at positions $\boldsymbol{R}_j$. These particles interact with each other via the long-range Coulomb forces and short-range interatomic forces, and the ion dynamics is obtained from the solution of Newton's equations of motion

$$M_j \ddot{\boldsymbol{R}}_j + \nabla_{\boldsymbol{R}_j} \sum_{j'} V_{jj'}(\boldsymbol{R}_j - \boldsymbol{R}_{j'}) = eZ_j\, \boldsymbol{E}_{\mathrm{el}}(\boldsymbol{R}_j,t). \quad (11)$$

Here $V_{jj'}$ is the potential between ions j and j', and $\boldsymbol{E}_{\mathrm{el}}$ is the electric field of the swift electron, whose temporal shape approximately corresponds to an impulselike impetus at time zero [23]. In our computational approach we use the fast multipole method [24] for an efficient evaluation of the long-range Coulomb interactions.

For the solution of Newton's equations of motion we employ a simple Verlet algorithm with a time step of 1 fs (Ref. [25]). In our simulations we additionally include dissipative forces $-\gamma M_j \dot{\boldsymbol{R}}_j$ to account for finite temperature effects or other environment couplings, with a typical value of $\hbar\gamma = 2$ meV. Every MD simulation starts with a relaxation of the ion geometry to the ground state, either using a quasi-Newton Broyden-Fletcher-Goldfarb-Shanno (BFGS) scheme [26] for the minimization of the potential energy or a time evolution in the presence of the dissipative forces described through γ.

Within our model description we can express the induced current distribution in the form

$$\boldsymbol{J}_{\mathrm{ind}}(\boldsymbol{r},t) = \sum_j \dot{\boldsymbol{R}}_j\, eZ_k \delta(\boldsymbol{r} - \boldsymbol{R}_j), \quad (12)$$

where the ion trajectories $\boldsymbol{R}_j(t)$ are computed subsequent to the initial impetus of the swift electron. Performing a Fourier transform $\boldsymbol{J}_{\mathrm{ind}}(\boldsymbol{r},\omega) = \int_0^\infty e^{i\omega t} \boldsymbol{J}(\boldsymbol{r},t)\, dt$, where the current distribution decays fast in time because of the damping term and the integral only extends over a final time interval, we can insert $\boldsymbol{J}_{\mathrm{ind}}(\boldsymbol{r},\omega)$ into Eq. (5) to obtain the EELS loss probability.

For sufficiently small cubes, consisting of only a few thousand atoms with corresponding cube lengths of a few nanometers, we can solve Newton's equations of motion also through diagonalization of the dynamic matrices. This approach is briefly sketched in Appendix D and is similar

to the lattice dynamics calculations discussed above and will be used further below to investigate the validity of additional approximations introduced in our MD approach.

C. Local dielectric description

Similarly to plasmonics simulations [21,27,28], inelastic bulk and surface phonon losses could be also modeled with a local dielectric description in terms of a Lorentzian oscillator model [29]

$$\varepsilon(q \to 0,\omega) = \varepsilon_\infty\left[1 + \frac{\omega_{\rm LO}^2 - \omega_{\rm TO}^2}{\omega_{\rm TO}^2 - \omega(\omega + i\eta)}\right], \qquad (13)$$

or some other form extracted from experiment. The limit $q \to 0$ is valid in the long wavelength regime. In the above expression $\omega_{\rm LO}$ and $\omega_{\rm TO}$ are the frequencies of the longitudinal and transversal optical phonons, respectively, η is a damping constant, and ε_∞ is the high-frequency permittivity of the ionic crystal. For the MgO cube, to be discussed further below, we solve Maxwell's equations in the quasistatic approximation together with the framework discussed in detail in Refs. [21,27,28]. In addition to the surface phonon losses suffered by the electron we must also introduce the bulk losses through a term [21]

$$P_{\rm bulk}(\hbar\omega) = \frac{2e^2L}{\pi\hbar v^2}\,\Im\mathrm{m}\left[-\frac{1}{\varepsilon(q \to 0,\omega)}\right]\ln\left(\frac{q_c v}{\omega}\right). \qquad (14)$$

In the above expression L is the distance traveled by the electron inside the ionic cube, and q_c is the cutoff wave number associated with the acceptance angle θ_m of the electron spectrometer.

As we have shown in Ref. [2] and will discuss in more detail below, the local dielectric description works perfectly well for electrons passing by the nanocube (aloof geometry), whereas for electron trajectories intersecting the cube Eq. (14) provides a poor description because it doesn't include short-wavelength phonon contributions.

III. RIGID-ION MODEL

In this paper we investigate inelastic vibrational bulk and surface losses of swift electrons in a MgO nanocube. For the interatomic forces we use a simple rigid-ion model with potentials taken from Matsui [18], see also Ref. [25] for related work. The phonon modes for this model are here computed for zero temperature (see Fig. 8 for the MgO phonon dispersion), and we obtain for small wave vectors TO and LO phonon energies of approximately 50 and 100 meV, which are somewhat larger than other values reported in the literature and observed in experiment. However, the purpose of our work is to compare the results of different approaches and we have thus given precedence to one set of consistent parameters to facilitate the comparison. Our probability calculations are performed for zero temperature, which produces statistical occupational factors for loss and gain scattering processes of one and zero, respectively.

In Sec. IV we employ the rigid-ion approximation for the description of the lattice dynamics in a MgO cube, using either a molecular dynamics (MD) or lattice dynamics (LD) approach. Figure 1 shows typical cubes for our simulations,

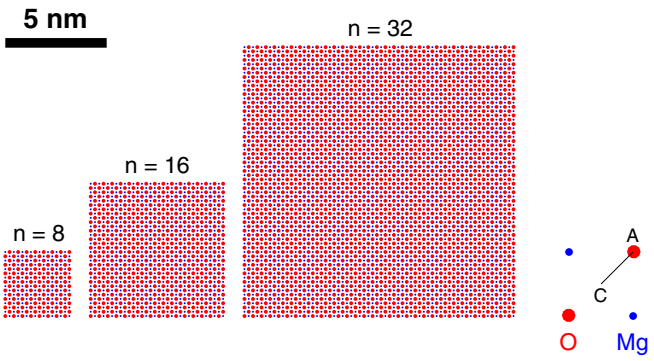

FIG. 1. Typical cube sizes used in our MD simulations with 8, 16, and 32 unit cells along each spatial dimension, consisting of Mg (blue) and O (red) ions. On the right of the figure we zoom into one unit cell and mark position A and the center C. In our simulations we usually vary the impact parameter $\boldsymbol{R}_0$ of the electron beam along the direction AC.

oriented along the [001] direction, consisting of 8, 16, or 32 unit cells per dimension. On the right of the figure we zoom into a single unit cell and mark position A and the center C. Below we will vary the impact parameter of the electron beam along the direction AC, expressing distances with respect to the position A.

We next investigate the validity of the rigid ion model and, in particular, our use of pointlike ions. We employ a simple description scheme using hydrogenlike atomic states for Mg and O, together with a $1/r$ electric field distribution for the swift electron [21], which is expected to be a suitable approximation for small distances r between the impact parameter $\boldsymbol{R}_0$ of the swift electron and the ion positions. For the two outer electrons of the O^{2-} ions we consider an isotropic charge distribution

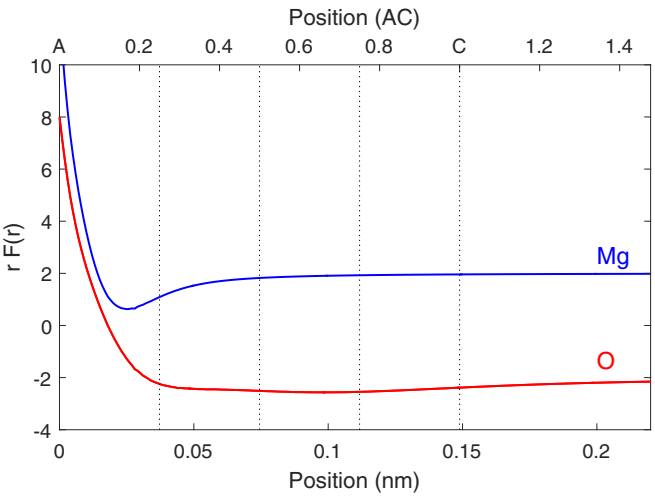

FIG. 2. Force $F(r)$ acting on a single ion as the impact parameter $\boldsymbol{R}_0$ is varied along the direction AC, indicated in Fig. 1, for realistic charge distribution of ions (for details see text). The force exerted by the electron beam has an approximate $1/r$ dependence [21], in the figure we plot $r\,F(r)$ rather than the force itself. For small distances the force approaches the atomic numbers of 12 e and 8 e for Mg and O, respectively, whereas for larger distances it approaches the effective ion charges of $\pm 2\,e$.

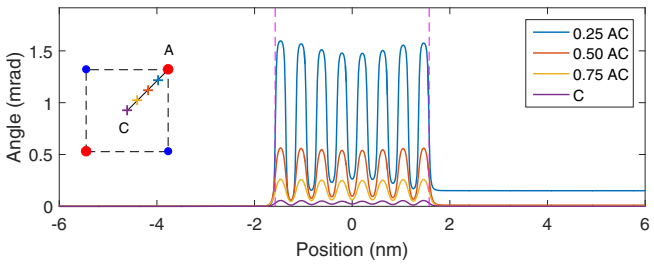

FIG. 3. Deflection angle of the electron velocity with respect to the forward direction while passing through a $n = 8$ MgO nanocube. We show the deflection angles in mrad for different impact parameters, corresponding to position C, as well as 75%, 50%, and 25% of direction AC shown in the inset. The vertical dashed lines indicate the cube boundaries.

suggested by Zuo *et al.* [30],

$$\rho(r) = -2e\,N\,r^n e^{-\alpha r}\,, \tag{15}$$

where $n = 5, \alpha = 9.04\,\text{Å}^{-1}$, and N is a normalization constant that depends on n and α. Figure 2 shows the force exerted by the electron beam on the Mg (blue) and O (red) ions, where we plot $r\,F(r)$ rather than the force itself to highlight the derivations from the simple $1/r$ dependence. For small distances the force approaches the atomic numbers of $12\,e$ and $8\,e$ for Mg and O, respectively, whereas for larger distances it approaches the effective ion charges of $\pm 2\,e$. From the figure we conclude that a pointlike ion charge distribution provides a viable description scheme for distances larger than say 0.05 nm, corresponding to approximately 60 percent of the AC distance, see Fig. 1. For smaller distances the detailed form of the ion charge distribution as well as polarization effects of the electron cloud should in principle be taken into account. For simplicity, in this paper we will also consider electron trajectories with impact parameters down to 25 percent of the AC distance, but the corresponding results should be considered with caution. A discussion of this point will be given in Sec. V.

In Fig. 3 we show results for a simulation based on Newton's equations of motion where a swift electron with a kinetic energy of 60 keV passes through a $n = 8$ nanocube, with the impact parameters around the cube center varied along the direction AC indicated in Fig. 1. We observe small deflection angles of the electron velocity with respect to the forward direction caused by the Coulomb forces of the ions. As detailed in Appendix A and discussed at length in Ref. [20], in our theoretical approach we assume straight trajectories without any deflection, an assumption approximately valid considering the overall small deflection angles in comparison to, e.g., the acceptance angle of 20 mrad of the electron collector used in experiment [2]. The above simulations thus support our simplified rigid-ion model together with a straight-line electron trajectory, at least for a semiquantitative modeling of the experiments.

IV. RESULTS

A. Local dielectric description

We first consider a local dielectric description for a 50 nm MgO nanocube, and compute the electron loss probabilities

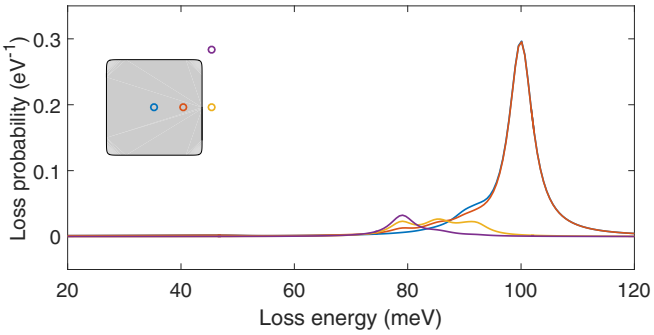

FIG. 4. Loss probability for a single 50 nm MgO nanocube and for an electron beam with a kinetic energy of 60 keV. The results are computed for various electron beam positions shown in the inset using a local dielectric description and the simulation software of Refs. [28,31]. We use the dielectric function of Eq. (13) with values of $\omega_{\text{TO}} = 50$ meV, $\omega_{\text{LO}} = 100$ meV, $\eta = 5$ meV, and $\varepsilon_\infty = 3$ representative for MgO (Ref. [32]). The peak at 100 meV is due to bulk losses to LO phonons, whereas the peaks at lower energies are due to surface phonon polariton excitations localized at the corners, edges, and faces of the cube. Note that for the intersecting geometries (red and blue lines) there are no excitations present below 60 meV.

using the simulation software of Refs. [28,31]. For the dielectric function $\varepsilon(q \to 0, \omega)$ we use the form of Eq. (13) with parameters representative for MgO, see caption of Fig. 4, which are chosen in accordance to our molecular dynamics and lattice dynamics simulations to be discussed below.

Figure 4 shows EELS spectra for selected impact parameters indicated in the inset. When the electron beam passes through the nanocube, the loss spectra consist of a major peak at 100 meV associated with losses to LO phonons, as computed from Eq. (14). In addition we observe at lower loss energies additional peaks which we attribute to surface phonon polaritons localized at the corners, edges, and faces of the cube. These excitations have been described in detail in Refs. [2,15,32] and will not be further discussed here. In striking disagreement with experiment we do not observe pronounced loss contributions at energies below say 60 meV, see Fig. 3 of Ref. [2]. As will be discussed below, these losses can be attributed to excitations of acoustic phonons with finite momentum exchange, which are missing in a local dielectric description with $q \to 0$. To account for such losses, we next employ molecular dynamics and lattice dynamics simulations based on the rigid ion approximation.

B. Molecular dynamics

We next discuss MD simulations, which start with a relaxation of the ion geometry to the ground state as discussed in Sec. II B. For sufficiently small nanocubes, we can then set up the dynamic matrix using the harmonic approximation and diagonalize it, as discussed in Appendix D. Figure 5(a) shows the phonon density of states (DOS) for the $n = 8$ cube shown in Fig. 1 on the left, Fig. 5(b) shows EELS spectra for selected impact parameters in the unit cell located in the cube center. As will be discussed below, the peaks at loss energies of approximately 35 meV and 50 meV can be primarily attributed to acoustic phonon excitations, the peaks in the range between

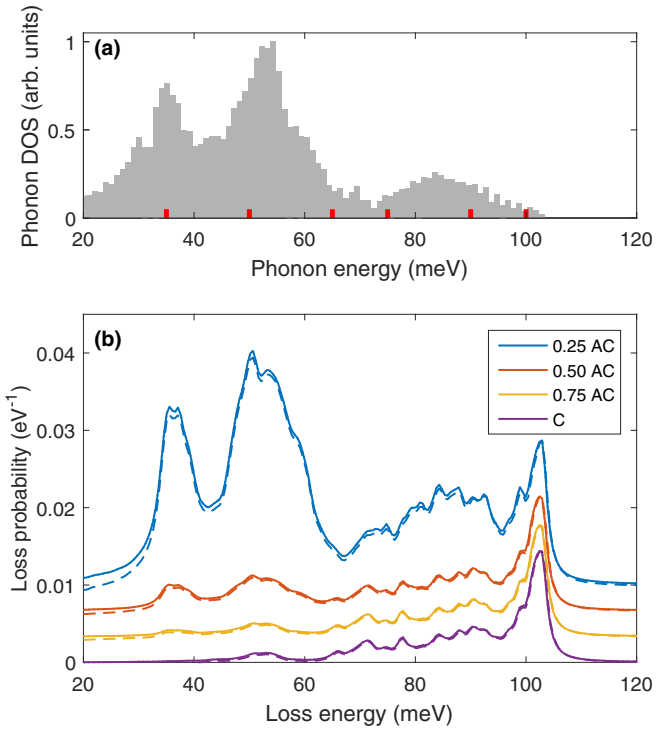

FIG. 5. Results for MD simulations and for a $n = 8$ nanocube. (a) Phonon density of states. (b) Loss probabilities for different impact parameters, see Fig. 1 for the location of the points A and C or inset of Fig. 3. Different spectra are offset for clarity. See text for a definition of the solid and dashed lines.

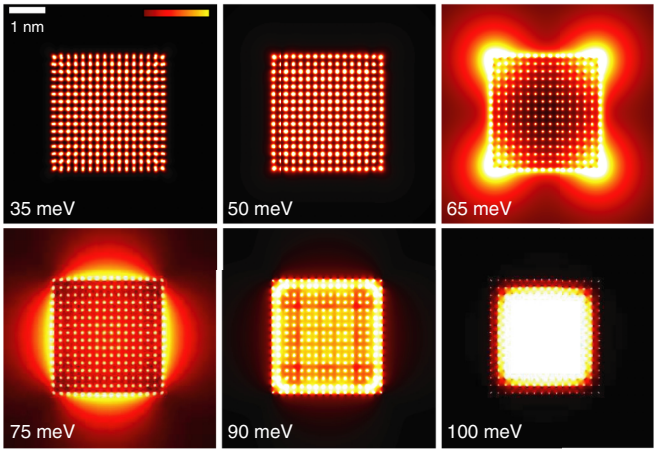

FIG. 6. EELS maps for $n = 8$ cube and for selected loss energies, indicated in Fig. 5(a). The maps at 35 meV and 50 meV correspond to acoustic phonon excitations, the maps at 65 meV and 75 meV correspond to edge and face surface phonon polaritons, respectively, and the maps at 90 meV and 100 meV correspond to LO phonon excitations. All maps are scaled with respect to the highest loss probabilities for a given loss energy.

60 meV and 80 meV lie in the reststrahlen band of the material [15] and can be associated with the excitation of surface phonon polaritons, and the peaks above 80 meV are due to optical phonons.

Before proceeding, we comment on a few technical points. First, we decompose the electric field of the electron beam, see Eq. (B1), into components perpendicular and parallel to the electron propagation direction z. When neglecting the z component of the electrical field and setting $k \to 0$ in Eq. (B1), the electric field becomes independent of ω and corresponds to the field produced by a charged wire located at the impact position $\boldsymbol{R}_0$ where the electric field points into the radial direction and decays with a simple $(1/r)$ dependence. The dotted lines in Fig. 5(b), indistinguishable from the solid ones, report results from such simulations and show that this approximation, which we have previously also used in Fig. 2, is extremely well justified for the fast electrons and small loss energies of our present concern. The dashed lines in the figure show results of simulations without the harmonic approximation where we solve Newton's equations of motion for the ion dynamics using the Verlet algorithm discussed in Sec. II B. This approach, which is needed for larger nanocubes where the storage and diagonalization of the dynamic matrix becomes unfeasible, gives practically undistinguishable results.

Figure 6 shows EELS maps for the $n = 8$ nanocube and for a few selected loss energies indicated by red bars in Fig. 5(a). Although the results for electron trajectories in closest vicinity to the ions should be treated with some care, the results show a number of features that we consider to be of general nature. First, the acoustic phonons at the lowest loss energies of 35 meV and 50 meV can only be excited for electron trajectories located in close proximity to the ion columns. A more quantitative analysis is shown in Fig. 5(b) where we observe that only for the distances below 0.50 AC the peaks of the acoustic phonons exceed the LO phonon peak around 100 meV. Second, the peaks around 65 meV and 75 meV, which have a very small density of states, see Fig. 5(a), have significant loss probabilities outside the nanocube. This result is in accordance to the simulations based on the local dielectric description, and we correspondingly assign the modes to surface phonon polaritons located at the corners, edges, and faces of the cube. Finally, the modes at the highest loss energies are attributed to LO phonon excitations. The mode at 90 meV is an oscillation located at the outermost atom layers of the cube, in agreement to the findings of Ref. [25], whereas the almost featureless map at 100 meV is attributed to the longitudinal-phonon bulk losses of Eq. (14) which have been previously discussed for the local dielectric description.

Finally, in Fig. 7(a) we show EELS spectra for MD simulations of $n = 16$ (dashed lines) and $n = 32$ (solid lines) nanocubes using the Verlet algorithm. We have divided the loss probabilities by the length L of the nanocube to facilitate a comparison between the two results. As can be seen, the acoustic phonon peak of lowest energy is almost independent for the different nanocube sizes, whereas the peak around 50 meV has a small L dependence. In contrast, the loss peaks associated with surface phonon polaritons around 70 meV and LO phonons around 100 meV depend decisively on L. The loss probability to LO phonons is in principle well described by P_{bulk} of Eq. (14) where $q = \omega/v$ is the momentum cutoff due to kinematic constraints [19,21]. When q becomes smaller than the smallest momentum π/L sustained by a nanocube, one should replace q in Eq. (14) by π/L such that $P_{\text{bulk}}/L \propto \ln(q_c L)$ becomes size dependent, in accordance to the results shown in Fig. 7(a).

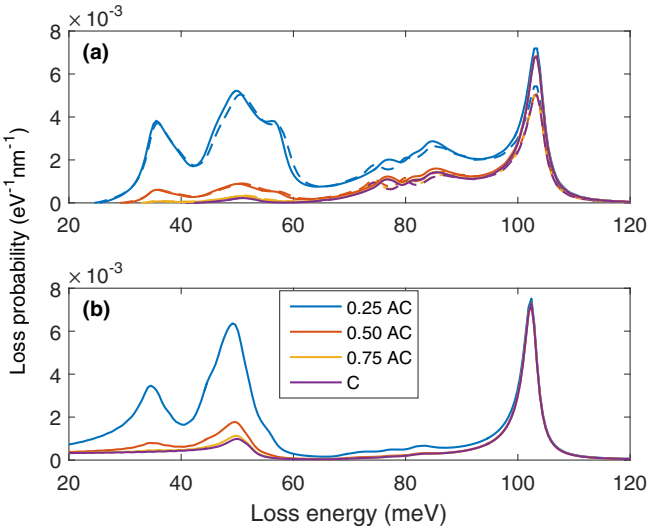

FIG. 7. EELS spectra for different impact parameters and for (a) finite MgO nanocube and (b) infinite crystal. (a) MD simulation results for $n = 16$ (dashed lines) and $n = 32$ (solid lines) nanocubes. The loss probabilities were scaled by the cube size to facilitate the comparison. (b) Results of LD calculations using Eq. (10), with data scaled by a factor of 0.8 to allow for identical axes in both panels. Note that only for the finite nanocubes surface phonon excitations are present in the 60–90 meV range.

C. Lattice dynamics

The lattice dynamics approach discussed in Sec. II A provides a means to compute the bulk losses inside the cube, but it cannot account for surface phonon polariton losses or the Begrenzung effect [19]. Figure 7(b) shows the EELS probability per unit length as computed from Eq. (10) and using the same material parameters as in the MD approach (harmonic approximation). The results agree well with the MD results, however, the acoustic phonon peak at 50 meV becomes even more pronounced, all surface phonon polariton contributions are missing in the energy range between 60 and 80 meV, and the LO phonon peak is stronger for the reasons discussed at the end of the previous section.

In the LD calculations we can now decompose the loss probability $P(\hbar\omega)$ of Eq. (10) into phonon modes with different wave numbers $\boldsymbol{q}$ and phonon energies $\omega_{\boldsymbol{q}\lambda}$. Figure 8 shows the relative weight for the two different impact parameters of (a) 0.50 and (b) 0.25 × AC. As can be inferred from the figure, for small wave numbers LO phonons contribute strongest to $P(\hbar\omega)$, whereas for larger wave numbers both longitudinal and transversal acoustic phonons acquire a significant weight. When summed over the entire two-dimensional Brillouin zone, which approximately agrees with the momentum exchange accessible by an electron spectrometer with a collection angle of 20 mrad, we obtain the loss spectra of Fig. 7(b).

Finally, we performed simulations where we integrate in Eq. (10) not over the entire Brillouin zone but introduce a wave number cutoff of say $q_{\text{cut}} \approx 0.1$ Å^{-1} to mimic the $q \to 0$ limit of the local dielectric description. The results (not shown) agree with those of the local dielectric description, Fig. 4, and the loss spectra consist of a single peak associated with LO phonon excitations.

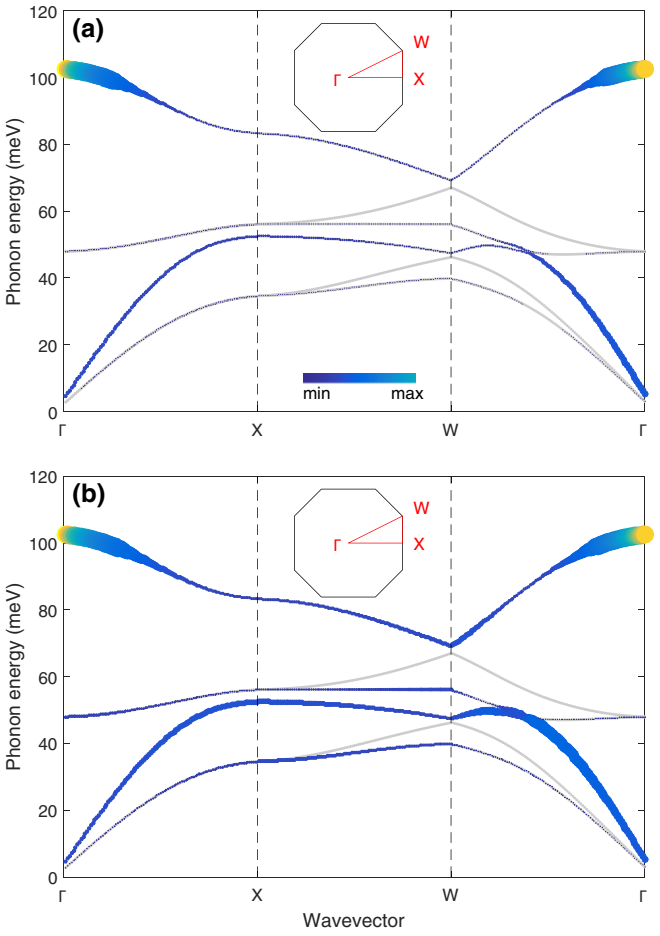

FIG. 8. Contribution of phonon modes to electron energy loss probability $P(\hbar\omega)$ of Eq. (10). The Brillouin zone and the path of the selected wave vectors are shown in the insets. We plot the contributions $|\mathcal{F}_\lambda(\boldsymbol{q})|^2$ to $P(\hbar\omega_{\boldsymbol{q}\lambda})$, see Eq. (10), using impact parameters of (a) 0.5× and (b) 0.25× AC. For better visibility, the sizes of the largest dots have been set to a maximum value.

V. SUMMARY AND DISCUSSION

To summarize, in this paper we have theoretically analyzed electron energy loss spectroscopy of phonons and phonon polaritons in a single ionic cube, using different description schemes based on either a local dielectric description or the rigid ion model.

Local dielectric description. Here the system is described in terms of a local dielectric function $\varepsilon(q \to 0, \omega)$, similar to related studies of bulk and surface plasmons in metallic nanostructures. This approach is well suited for the simulation of aloof geometries, with electron losses caused by surface phonon polaritons, and to intersecting geometries where the electron moves sufficiently far away from the ion columns and the loss is predominantly due to Coulombic long-range interactions with LO phonons. On the other hand, when the electron trajectories are closer to the ions this approach completely fails to reproduce losses to acoustic and TO phonons.

Molecular dynamics simulations. For sufficiently small nanocubes one can simulate the ion dynamics using Newton's equations of motion for parametrized interatomic forces. This

approach has the advantage that it uses only a small number of approximations and thus accounts for effects such as surface or bulk losses, as well as localized phonons and the Begrenzung effect on the same footing. On the other hand, simulations become computationally prohibitively difficult for larger nanostructures.

Lattice dynamics simulations. Here the phonon dynamics is described for an infinitely large crystal, using interatomic forces and ion form factors at various degrees of sophistication. By construction, this approach can only describe bulk losses, but it cannot account for surface phonon losses or the Begrenzung effect. Computationally, lattice dynamics simulations are significantly more simple than molecular dynamics simulations, and the approach makes direct contact with phonon modes and dispersions commonly employed in solid state physics.

In this paper we have presented relatively simple implementations of the different approaches. As for the molecular and lattice dynamics simulations we have found fairly good agreement, which allows us to draw a number of general conclusions. First, for intersection geometries where the electron moves sufficiently far away from the ions the loss spectra are governed by long-range Coulomb interactions with LO phonons, which could be also modelled within a local dielectric description. When the swift electron moves closer to the ions, losses to acoustic and TO phonons become of increasing importance. Finally, for extremely close trajectories the loss spectra are governed by the complete phonon spectra, although the results have to be handled with some care due to possible failures of our simplified rigid ion description. Quite generally, in experiment the location of the electron beam spatially varies on the sub-Angstrom level, due to diffraction and channeling conditions in the crystal, and the loss spectra thus become a convolution of various beam locations.

We foresee several improvements for our theoretical approach, which will be investigated in more detail in future work. First, although conceptually easy, the rigid ion approximation is probably too simple for a truly quantitative comparison. Atomistic descriptions schemes based on density functional theory or variants could provide more accurate phonon energies and eigenvectors, as well as the form factors for the ionic charge distributions. Second, temperature effects, such as phonon occupations or thermal lattice expansion, should be included. In particular the inclusion of thermal occupations is conceptually simple and has been already briefly mentioned in Sec. II, and also its implementation should be rather straightforward. Finally, one should go beyond the semiclassical description of electron-ion losses and include a more realistic wave-function description for the propagating electron, possibly including multiple phonon interactions. We also believe that different material systems, including hybrid structures and interfaces, will be interesting candidates for both future experimental and theoretical investigations.

ACKNOWLEDGMENTS

This work has been supported in part by the Austrian science fund FWF under the SFB F49 NextLite (F4906-N23), project P27299–N27, and NAWI Graz. P.E.B. and M.J.L would like to acknowledge the financial support of U.S. Department of Energy, Office of Science, Basic Energy Sciences under Award No. DE-SC0005132.

APPENDIX A

In this Appendix we show how to derive our central expression of Eq. (5). We start by explicitly working out the square modulus $|\dots|^2$ in Eq. (3) and multiply the expression between the vertical bars by its complex conjugate. With the susceptibility of Eq. (4) and the decomposition of the transition rate into loss energies, described in the main text, we are then led to

$$\gamma(\hbar\omega) = 2e^2 \sum_{f,n} \int \psi_f(\boldsymbol{r})\psi_i^*(\boldsymbol{r})\Im\mathrm{m}[-W_{\mathrm{ind}}(\boldsymbol{r},\boldsymbol{r}',\omega)] \times \psi_f^*(\boldsymbol{r}')\psi_i(\boldsymbol{r}')\, d^3r d^3r'\, \delta(\hbar\omega + \varepsilon_f - \varepsilon_i)\,, \quad \text{(A1)}$$

where we have introduced the screened Coulomb interaction [21]

$$W_{\mathrm{ind}}(\boldsymbol{r},\boldsymbol{r}',\omega) = \int \frac{\chi(\boldsymbol{r}_1,\boldsymbol{r}_2,\omega)}{|\boldsymbol{r}-\boldsymbol{r}_1|\,|\boldsymbol{r}_2-\boldsymbol{r}'|}\, d^3r_1 d^3r_2\,. \quad \text{(A2)}$$

Equation (A1) allows for a transparent interpretation of the electron energy loss: An electron density fluctuation $\psi_f^*(\boldsymbol{r}')\psi_i(\boldsymbol{r}')$ couples via the bare Coulomb potential to the ionic system, where it propagates for a while, as described by the density-density correlation $\chi(\boldsymbol{r},\boldsymbol{r}',\omega)$, and finally couples back to the electron density fluctuation. Through this self-interaction process the electron transfers a tiny fraction of its kinetic energy to the ionic system resulting in an electron energy loss.

It is convenient to make a number of additional approximations in Eq. (A1). First, we consider an initial electron wave packet $\psi_i(\boldsymbol{r}) = e^{ik_i z}\phi_\perp(\boldsymbol{R})/\sqrt{L}$ with central wave number k_i that propagates along the z direction, where L is the quantization length of the electron trajectory. $\phi_\perp(\boldsymbol{R})$ is the wave function in the transversal direction $\boldsymbol{R}$, and we ignore dispersion along $\boldsymbol{R}$ (see Ref. [20] for details). The final states are expressed in terms of plane waves $\psi_f(\boldsymbol{r}) = e^{i\boldsymbol{k}_f\cdot\boldsymbol{r}}$ and we neglect in the energy conservation

$$\hbar\omega = \varepsilon_i - \varepsilon_f = \hbar v(k_i - k_{fz}) + \frac{\hbar^2 k_f^2}{2m} \approx \hbar v(k_i - k_{fz})$$

the recoil term $\hbar^2 k_f^2/(2m)$, where k_{fz} denotes the z component $\boldsymbol{k}_f$ and m is the free electron mass. The transition probability $P(\hbar\omega)$ is obtained from the transition rate $\gamma(\hbar\omega)$ by multiplying with the interaction time L/v, where v is the electron velocity, and we are led to

$$P(\hbar\omega) = \frac{2e^2}{v}\int \frac{d^3k_f}{(2\pi)^3}\int d^3r d^3r' e^{i\boldsymbol{k}_f\cdot\boldsymbol{r}}\phi_\perp^*(\boldsymbol{R})e^{-ik_i z} \times \Im\mathrm{m}[-W_{\mathrm{ind}}(\boldsymbol{r},\boldsymbol{r}',\omega)]e^{-i\boldsymbol{k}_f\cdot\boldsymbol{r}'}\phi_\perp(\boldsymbol{R}')e^{ik_i z'} \times \delta(\hbar\omega - \hbar v[k_i - k_{fz}])\,.$$

The z component of k_{fz} is then determined by Dirac's delta function. As discussed in some detail in Ref. [20], the integration over $\boldsymbol{k}_{f\perp}$ should only extend over the finite acceptance angle θ_m of the electron microscope. However, for kinetic electron energies in the 100 keV range and $\theta_m \gg 1$ mrad one

can safely use the following approximation [20]

$$\int e^{i\boldsymbol{k}_f\cdot(\boldsymbol{R}-\boldsymbol{R}')}\,d^2k_f \approx (2\pi)^2\delta(\boldsymbol{R}-\boldsymbol{R}')\,.$$

Thus, we are finally led to

$$P(\omega) = \frac{e^2}{\pi\hbar v^2}\int |\phi_\perp(\boldsymbol{R})|^2 \times e^{i\frac{\omega}{v}(z'-z)}\mathfrak{Im}[-W_{\rm ind}(\boldsymbol{r},\boldsymbol{r}',\omega)]\,d^2R dz dz'\,. \quad \text{(A3)}$$

If the transversal extension of the electron beam is strongly peaked around the impact parameter $\boldsymbol{R}_0$ we obtain the even more simple expression

$$P(\omega) = \frac{e^2}{\pi\hbar v^2}\int e^{i\frac{\omega}{v}(z'-z)} \times \mathfrak{Im}[-W_{\rm ind}(\boldsymbol{R}_0,z,\boldsymbol{R}_0,z',\omega)]\,dz dz'\,. \quad \text{(A4)}$$

We have repeated this derivation, which can be also found in Refs. [20,21], to emphasize the following points. First, Eqs. (A3) and (A4) are based on a genuine quantum description subject to the approximations described above. In the main text we critically examine these approximations, in particular for electrons propagating in close vicinity of the ions. Second, our central equations can be used for any kind of environment couplings, such as to plasmons or phonons, where all details of the environment are hidden in the susceptibility or the screened Coulomb interaction.

Equation (A4) can be cast to a form more suitable for simulations. First, we note that for an electron propagating with velocity v along the z direction the Fourier transform of the charge distribution reads [21] $\rho_{\rm el}(\boldsymbol{r},\omega) = -\frac{e}{v}\delta(\boldsymbol{R}-\boldsymbol{R}_0)e^{i\omega z/v}$. With the induced charge distribution

$$\rho_{\rm ind}(\boldsymbol{r},\omega) = \int \frac{\chi(\boldsymbol{r},\boldsymbol{r}_1,\omega)\rho_{\rm el}(\boldsymbol{r}_2,\omega)}{|\boldsymbol{r}_1-\boldsymbol{r}_2|}\,d^3r_1 d^3r_2$$

the loss probability of Eq. (A4) can then be brought to the form

$$P(\hbar\omega) = -\frac{1}{\pi\hbar}\int \mathfrak{Im}[\phi^*_{\rm el}(\boldsymbol{r},\omega)\rho_{\rm ind}(\boldsymbol{r},\omega)]\,d^3r\,, \quad \text{(A5)}$$

which can be directly used for simulations based on a local dielectric description. Here we have introduced the scalar potential $\phi_{\rm el}(\boldsymbol{r},\omega) = \int \rho_{\rm el}(\boldsymbol{r}',\omega)/|\boldsymbol{r}-\boldsymbol{r}'|\,d^3r'$ of the swift electron.

For the explicit consideration of the phonon dynamics we proceed further and use the continuity equation $i\omega\rho = \nabla\cdot\boldsymbol{J}$ to relate the charge distribution to the current distribution. This gives

$$P(\hbar\omega) = \frac{1}{\pi\hbar\omega}\int \mathfrak{Re}[\phi^*_{\rm el}(\boldsymbol{r},\omega)\nabla\cdot\boldsymbol{J}_{\rm ind}(\boldsymbol{r},\omega)]\,d^3r\,.$$

We next perform integration by parts to bring the derivative from the second term to the first one. Using that $\boldsymbol{J}_{\rm ind}(\boldsymbol{r},\omega)$ becomes zero for $r\to\infty$ and introducing the electric field $\boldsymbol{E}_{\rm el}(\boldsymbol{r},\omega) = -\nabla\phi_{\rm el}(\boldsymbol{r},\omega)$, we are led to our final expression of Eq. (5).

APPENDIX B

In this Appendix we compute the Fourier transform of the electric field for a swift electron [21]

$$\boldsymbol{E}_{\rm el}(\boldsymbol{r},\omega) = \frac{ie}{\pi}\int e^{i\boldsymbol{q}\cdot(\boldsymbol{r}-\boldsymbol{R}_0)}\left[\frac{\boldsymbol{q}-k\frac{\boldsymbol{v}}{c}}{q^2-k^2}\right]\delta(\omega-\boldsymbol{q}\cdot\boldsymbol{v})\,d^3q\,, \quad \text{(B1)}$$

where $k=\frac{\omega}{c}$ is the wave number of light. For an electron propagating along z we can evaluate Dirac's delta function and obtain

$$\boldsymbol{E}_{\rm el}(\boldsymbol{r},\omega) = \frac{ie}{\pi v}\int e^{i\boldsymbol{q}\cdot(\boldsymbol{r}-\boldsymbol{R}_0)}\boldsymbol{e}(\boldsymbol{q})\,d^2q_\perp\,, \quad \text{(B2)}$$

where we have decomposed $\boldsymbol{q}=(\boldsymbol{q}_\perp,\frac{\omega}{v})$ into the components perpendicular and parallel to the electron propagation direction. $\boldsymbol{e}(\boldsymbol{q})$ is the expression given in the brackets of Eq. (B1).

In the lattice dynamics approach we will additionally need the wave-vector decomposition of the electric field

$$\boldsymbol{E}_{\rm el}(\kappa,\boldsymbol{q}) = \frac{1}{N}\sum_\ell e^{-i\boldsymbol{q}\cdot\boldsymbol{R}_\ell}\boldsymbol{E}_{\rm el}(\boldsymbol{R}_\ell+\boldsymbol{r}_\kappa,\omega)\,, \quad \text{(B3)}$$

where N is the total number of unit cells. Inserting Eq. (B2) into Eq. (B3) gives

$$\boldsymbol{E}_{\rm el}(\kappa,\boldsymbol{q}) = \frac{ie}{\pi vN}\sum_\ell\int e^{-i\boldsymbol{q}\cdot\boldsymbol{R}_\ell}e^{i\boldsymbol{q}'\cdot(\boldsymbol{r}_\kappa-\boldsymbol{R}_0)}\boldsymbol{e}(\boldsymbol{q})\,d^2q'_\perp\,,$$

where $\sum_\ell e^{i(\boldsymbol{q}'-\boldsymbol{q})\cdot\boldsymbol{R}_\ell} = N\delta_{\boldsymbol{q}'-\boldsymbol{q},\boldsymbol{G}}$ accounts for momentum conservation modulo a reciprocal lattice vector $\boldsymbol{G}$. We then arrive at our final expression

$$\boldsymbol{E}_{\rm el}(\kappa,\boldsymbol{q}) = \frac{ie}{\pi v}\left(\frac{2\pi}{L}\right)^2\sum_{\boldsymbol{G}} e^{i(\boldsymbol{q}+\boldsymbol{G})\cdot(\boldsymbol{r}_\kappa-\boldsymbol{R}_0)}\boldsymbol{e}(\boldsymbol{q}+\boldsymbol{G})\,, \quad \text{(B4)}$$

where we have implicitly assumed $q_z=\frac{\omega}{v}$ and $G_z=0$. L is the quantization length of the crystal, which we let approach infinity at the end of our calculation, and the additional factor of $(\frac{2\pi}{L})^2$ originates from the replacement of Kronecker's delta for momentum conservation by Dirac's delta function in the limit of $L\to\infty$.

For the sake of completeness we prove that indeed the inverse transformation

$$\boldsymbol{E}_{\rm el}(\boldsymbol{R}_\ell+\boldsymbol{r}_\kappa,\omega) = \sum_{\boldsymbol{q}} e^{i\boldsymbol{q}\cdot\boldsymbol{R}_\ell}\boldsymbol{E}_{\rm el}(\kappa,\boldsymbol{q})$$

holds. Replacing the summation over $\boldsymbol{q}$ by an integration over the first Brillouin zone we get

$$\frac{ie}{\pi v}\sum_{\boldsymbol{G}}\int_{BZ} e^{i(\boldsymbol{q}+\boldsymbol{G})\cdot(\boldsymbol{R}_\ell+\boldsymbol{r}_\kappa-\boldsymbol{R}_0)}\boldsymbol{e}(\boldsymbol{q}+\boldsymbol{G})\,d^2q_\perp\,.$$

We next combine the summation over the reciprocal lattice vectors and the integration over $\boldsymbol{q}_\perp$ to an unrestricted wave-vector integration and obtain our final expression

$$E_{\rm el}(\boldsymbol{R}_\ell+\boldsymbol{r}_\kappa,\omega) = \frac{ie}{\pi v}\int e^{i\boldsymbol{q}\cdot(\boldsymbol{R}_\ell+\boldsymbol{r}_\kappa-\boldsymbol{R}_0)}\boldsymbol{e}(\boldsymbol{q})\,d^2q_\perp\,,$$

which is the same as Eq. (B2). This completes our proof.

APPENDIX C

In this Appendix we derive Newton's equations of motion in the harmonic approximation and show how to arrive at Eq. (7) of the main text. We assume that the ion displacements $\boldsymbol{u}(\kappa,\ell)$ from the equilibrium positions $\boldsymbol{R}_\ell + \boldsymbol{r}_\kappa$ are sufficiently small such that we can expand the potential term in Newton's equations of motion to obtain [33]

$$-\omega^2 M_\kappa \boldsymbol{u}(\kappa,\ell) + \sum_{\kappa'\ell'} \boldsymbol{\Phi}(\kappa,\kappa',\boldsymbol{R}_\ell - \boldsymbol{R}_{\ell'}) \cdot \boldsymbol{u}(\kappa',\ell') = e Z_\kappa \, \boldsymbol{E}_{\rm el}(\boldsymbol{R}_\ell + \boldsymbol{r}_\kappa,\omega)\,, \tag{C1}$$

where $\boldsymbol{\Phi}$ is the usual force constant matrix of lattice dynamics [34]. It is convenient to introduce a wave-vector decomposition for the lattice displacements $\boldsymbol{U}(\kappa,\boldsymbol{q}) = N^{-1}\sum_\ell e^{-i\boldsymbol{q}\cdot\boldsymbol{R}_\ell}\boldsymbol{u}(\kappa,\ell)$ and we are led to

$$-\omega^2 M_\kappa \boldsymbol{U}(\kappa,\boldsymbol{q}) + \sum_{\kappa'\ell} e^{-i\boldsymbol{q}\cdot\boldsymbol{R}_\ell}\boldsymbol{\Phi}(\kappa,\kappa',\boldsymbol{R}_\ell)\cdot\boldsymbol{U}(\kappa,\boldsymbol{q}) = e Z_\kappa \boldsymbol{E}_{\rm el}(\kappa,\boldsymbol{q})\,, \tag{C2}$$

with the electric field given by Eq. (B4). To solve Eq. (C2) we introduce mass-weighted coordinates $\boldsymbol{\xi}(\kappa,\boldsymbol{q}) = M_\kappa^{1/2}\boldsymbol{U}(\kappa,\boldsymbol{q})$ and compute the eigenvalues $\omega^2_{\boldsymbol{q}\lambda}$ and eigenvectors $\boldsymbol{\xi}_\lambda(\kappa,\boldsymbol{q})$ of the dynamic matrix,

$$\sum_{\kappa'\ell}(M_\kappa M_{\kappa'})^{-1/2} e^{-i\boldsymbol{q}\cdot\boldsymbol{R}_\ell}\boldsymbol{\Phi}(\kappa,\kappa',\boldsymbol{R}_\ell)\cdot\boldsymbol{\xi}_\lambda(\kappa,\boldsymbol{q}) = \omega^2_{\boldsymbol{q}\lambda}\,\boldsymbol{\xi}_\lambda(\kappa,\boldsymbol{q})\,. \tag{C3}$$

The dynamic matrix contains both short-range interatomic potentials and long-range Coulomb potentials, the latter being evaluated through an Ewald summation following the procedure discussed in Ref. [17]. Because the dynamic matrix is symmetric the eigenvectors $\boldsymbol{\xi}_\lambda(\kappa,\boldsymbol{q})$ form an orthonormal basis and allow us to solve Eq. (C1) in the form

$$\boldsymbol{U}(\kappa,\boldsymbol{q}) = M_\kappa^{-1/2}\sum_\lambda \frac{F_\lambda(\boldsymbol{q})}{\omega^2_{\boldsymbol{q}\lambda} - \omega(\omega+i\eta)}\,\boldsymbol{\xi}_\lambda(\kappa,\boldsymbol{q})\,, \tag{C4}$$

where we have introduced a small damping constant η to account for environment effects together with the abbreviation $F_\lambda(\boldsymbol{q}) = \sum_\kappa \boldsymbol{\xi}^*_\lambda(\kappa,\boldsymbol{q})\cdot M_\kappa^{-1/2} e Z_\kappa \, \boldsymbol{E}_{\rm el}(\kappa,\boldsymbol{q})$. This expression forms the starting point of the analysis presented in Sec. II A.

APPENDIX D

In this Appendix we show how to solve Newton's equations of motion for a finite cube within the harmonic approximation. The ions are located at positions $\boldsymbol{R}_j = \boldsymbol{R}^0_j + \boldsymbol{u}(j)$, with $\boldsymbol{R}^0_j$ being the equilibrium position of ion j and $\boldsymbol{u}(j)$ its displacement from equilibrium. In the harmonic approximation we assume that the displacements are sufficiently small such that we can expand the potential term in Eq. (11) around the equilibrium positions $\boldsymbol{R}^0$ in powers of $\boldsymbol{u}$. Noting that in equilibrium the first-order derivative vanishes and assuming a harmonic time dependence $e^{-i\omega t}\boldsymbol{u}$, we obtain

$$-\omega^2 M_j \boldsymbol{u}(j) + \sum_{j'} \boldsymbol{\Phi}(j,j')\cdot\boldsymbol{u}(j') = e Z_j \, \boldsymbol{E}_{\rm el}\big(\boldsymbol{R}^0_j,\omega\big)\,, \tag{D1}$$

where $\boldsymbol{\Phi}$ is the force constant matrix. To solve Eq. (D1) it is convenient to introduce mass-weighted coordinates $\boldsymbol{\xi}(j) = M_j^{1/2}\boldsymbol{u}(j)$ and to seek for the eigenvalues ω^2_λ and eigenvectors $\boldsymbol{\xi}_\lambda(j)$ of the dynamic matrix

$$\sum_{j'}(M_j M_{j'})^{-1/2}\boldsymbol{\Phi}(j,j')\cdot\boldsymbol{\xi}_\lambda(j') = \omega^2_\lambda\,\boldsymbol{\xi}_\lambda(j)\,. \tag{D2}$$

Because the dynamic matrix is symmetric the eigenvectors $\boldsymbol{\xi}_\lambda(j)$ form an orthonormal basis and allow us to solve Eq. (D1) in the form

$$\boldsymbol{u}(j) = M_j^{-1/2}\sum_\lambda \frac{F_\lambda}{\omega^2_\lambda - \omega(\omega+i\eta)}\,\boldsymbol{\xi}_\lambda(j)\,, \tag{D3}$$

where we have introduced a small damping constant η to account for environment effects together with the abbreviation $F_\lambda = \sum_j \boldsymbol{\xi}^*_\lambda(j)\cdot M_j^{-1/2} e Z_j \, E_{\rm el}(\boldsymbol{R}^0_j,\omega)$. To obtain the energy loss probabilities we proceed in complete analogy to the discussion given in Sec. II A and finally obtain an expression similar to Eq. (8) with the only difference that the wave number $\boldsymbol{q}$ has to be replaced by the ion index j.

[1] O. L. Krivanek, T. C. Lovejoy, N. Dellby, T. Aoki, R. W. Carpenter, P. Rez, E. Soignard, J. Zhu, P. E. Batson, M. J. Lagos *et al.*, Nature (London) **514**, 209 (2014).
[2] M. J. Lagos, A. Trügler, U. Hohenester, and P. E. Batson, Nature (London) **543**, 529 (2017).
[3] R. J. Glauber, Phys. Rev. **98**, 1692 (1955).
[4] J. J. Earney, Philos. Mag. **23**, 577 (1971).
[5] P. Rez, Microsc. Microanal. **20**, 671 (2014).
[6] B. D. Forbes and L. J. Allen, Phys. Rev. B **94**, 014110 (2016).
[7] C. Dwyer, Phys. Rev. B **89**, 054103 (2014).
[8] J. R. M. Saavedra and F. J. García de Abajo, Phys. Rev. B **92**, 115449 (2015).
[9] R. Ruppin and R. Englman, Rep. Prog. Phys. **33**, 149 (1970).
[10] D. L. Mills and E. Burstein, Rep. Prog. Phys. **37**, 817 (1974).
[11] D. Pines and P. Nozieres, *The Theory of Quantum Liquids* (Perseus Books, Massachusetts, 1999).
[12] C. Oshima, T. Aizawa, R. Souda, and Y. Ishizawa, Solid State Commun. **73**, 731 (1990).
[13] R. F. Wallis, D. L. Mills, and A. A. Maradudin, *Localized Excitations in Solids* (Plenum Press, New York, 1968).
[14] A. A. Lucas, J. Chem Phys. **48**, 3156 (1968).
[15] M. J. Lagos, A. Trügler, V. Amarasinghe, L. C. Feldman, U. Hohenester, and P. E. Batson, Microscopy (suppl 1) **67**, i3 (2018).
[16] P. Lambin, P. Senet, and A. A. Lucas, Phys. Rev. B **44**, 6416 (1991).
[17] E. W. Kellermann, Philos. Trans. R. Soc. London **238**, 63 (1940).
[18] M. Matsui, J. Chem. Phys. **91**, 489 (1989).
[19] R. H. Ritchie, Phys. Rev. **106**, 874 (1957).
[20] R. H. Ritchie and A. Howie, Philos. Mag. A **5**, 753 (1988).

[21] F. J. García de Abajo, Rev. Mod. Phys. **82**, 209 (2010).
[22] P. Nozières, *Theory of Interacting Fermi Systems* (Benjamin, New York, 1964).
[23] J. D. Jackson, *Classical Electrodynamics* (Wiley, New York, 1999).
[24] R. Coifman, V. Rokhlin, and S. Wandzura, IEEE Antennas and Propagation Magazine **35**, 7 (1993).
[25] Y. Chalopin, H. Dammak, M. Hayoun, M. Besbes, and J.-J. Greffet, Appl. Phys. Lett. **100**, 241904 (2012).
[26] D. P. Bertsekas, *Nonlinear Programming* (Athena Scientific, Cambridge, UK, 1999).
[27] F. J. García de Abajo and A. Howie, Phys. Rev. B **65**, 115418 (2002).
[28] U. Hohenester, Comput. Phys. Commun. **185**, 1177 (2014).
[29] T. Fujiwara and K. Ohtaka, J. Phys. Soc. Jpn. **24**, 1326 (1968).
[30] J. M. Zuo, M. O'Keeffe, P. Rez, and J. C. H. Spence, Phys. Rev. Lett. **78**, 4777 (1997).
[31] U. Hohenester and A. Trügler, Comput. Phys. Commun. **183**, 370 (2012).
[32] H. Lourenco-Martins and M. Kociak, Phys. Rev. X **7**, 041059 (2017).
[33] P. Senet, P. Lambin, J.-P. Vigneron, I. Derycke, and A. A. Lucas, Surf. Science **226**, 307 (1990).
[34] N. W. Ashcroft and N. D. Mermin, *Solid State Physics* (Saunders, Fort Worth, 1976).